Dynamics and Energetics of Trapped Diurnal Internal Kelvin Waves around a Midlatitude Island

Eiji Masunaga

Center for Water Environmental Studies, Ibaraki University, Mito, Japan

Oliver B. Fringer

*The Bob and Norma Street Environmental Fluid Mechanics Laboratory, Department of Civil
and Environmental Engineering, Stanford University, Stanford, California*

Yujiro Kitade

Department of Ocean Sciences, Tokyo University of Marine Science and Technology, Tokyo, Japan

Hidekatsu Yamazaki

*Department of Ocean Sciences, Tokyo University of Marine Science and Technology, and CREST,
Japan Science and Technology Agency, Tokyo, Japan*

Scott M. Gallager

Woods Hole Oceanographic Institution, Woods Hole, Massachusetts

ABSTRACT

The generation of trapped and radiating internal tides around Izu-Oshima Island located off Sagami Bay, Japan, is investigated using the three-dimensional Stanford Unstructured Nonhydrostatic Terrain-following Adaptive Navier–Stokes Simulator (SUNTANS) that is validated with observations of isotherm displacements in shallow water. The model is forced by barotropic tides, which generate strong baroclinic internal tides in the study region. Model results showed that when diurnal K_1 barotropic tides dominate, resonance of a trapped internal Kelvin wave leads to large-amplitude internal tides in shallow waters on the coast. This resonance produces diurnal motions that are much stronger than the semidiurnal motions. The weaker, freely propagating, semidiurnal internal tides are generated on the western side of the island, where the M_2 internal tide beam angle matches the topographic slope. The internal wave energy flux due to the diurnal internal tides is much higher than that of the semidiurnal tides in the study region. Although the diurnal internal tide energy is trapped, this study shows that steepening of the Kelvin waves produces high-frequency internal tides that radiate from the island, thus acting as a mechanism to extract energy from the diurnal motions.

1. Introduction

Internal waves are ubiquitous in the ocean and key to understanding Earth's climate system (Munk and Wunsch 1998) and can significantly contribute to transport of heat, salt, energy, sediment, and organic material in the ocean (Walsh 1991; Nakatsuka et al. 2004; Sharples et al. 2009). Continental shelves and shallow coastal areas are known as ''hot spots'' of internal tide generation (Cacchione et al. 2002; Carter and Gregg 2002). Tidally generated baroclinic internal waves, or internal tides, become highly nonlinear when they propagate into shallow areas. Such nonlinear internal waves can induce strong currents and instability leading to significant turbulent mixing in coastal areas (Richards et al. 2013; Masunaga et al. 2015). Recent studies reported that internal wave breaking contributes to transport and mixing of sediments and nutrients in coastal oceans (McPhee-Shaw 2006; Richards et al. 2013; Masunaga et al. 2015). Such

Corresponding author: Hidekatsu Yamazaki, hide@kaiyodai.ac.jp

mass transport due to internal waves is known as an important mechanism for maintaining ocean ecosystems (e.g., McPhee-Shaw 2006).

At midlatitudes, the inertial frequency $f = 2\Omega \sin\phi$, where Ω is the Earth's angular velocity and ϕ is the local latitude, is greater than the diurnal frequency and less than semidiurnal frequency. Internal waves with frequencies higher than the local inertial frequency (superinertial frequency) satisfy the dispersion relation

$$s = \frac{k}{m} = \sqrt{\frac{\omega^2 - f^2}{N^2 - \omega^2}}, \qquad (1)$$

where s is the internal wave characteristic slope; k and m are the horizontal and vertical wavenumber, respectively; ω is the wave frequency; and N is the buoyancy frequency defined by

$$N = \sqrt{-\frac{g}{\rho_0}\frac{d\rho}{dz}}, \qquad (2)$$

where g is the gravitational acceleration, ρ is the density, and z is the vertical coordinate. Because semidiurnal internal tides (e.g., S_2 or M_2 tides) are superinertial, they satisfy the dispersion relation [(1)].

The behavior of internal tides with characteristic slope s from (1) interacting with the topography of slope γ has been studied extensively (e.g., Thorpe 1987; Dauxois and Young 1999). For subcritical slopes ($\gamma < s$), internal waves can propagate into shallow areas leading to wave energy convergence (transmissive condition). For supercritical slopes ($\gamma > s$), internal wave energy reflects when the internal wave beam angle is smaller than the local topographic slope (reflective condition). For critical slopes ($\gamma = s$), the internal wave beam angle matches the topographic slope and leads to nonlinear internal wave motions, turbulence, and mixing (e.g., Thorpe 1998; Cacchione et al. 2002).

In contrast to semidiurnal tides, diurnal (subinertial frequency) internal tides do not satisfy the dispersion relation [(1)] at midlatitudes, since the diurnal frequency is lower than the inertial frequency. Such subinertial waves can only propagate as Kelvin waves along coasts and are referred to as perfect, Kelvin-trapped waves (Longuet-Higgins 1969, 1970) that propagate with the coast to their right (left) in the Northern (Southern) Hemisphere (Gill and Clarke 1974). One of the primary sources of subinertial waves is low-frequency wind fluctuations. It is well known that basin-scale internal Kelvin waves in stratified lakes are driven by wind stresses (Saggio and Imberger 1998; Auger et al. 2013). Kitade and Matsuyama (2000) reported that winds generate coastally trapped waves along the Japan coast.

Around islands, subinertial waves are trapped and can be resonant when the circumference of the island is an integer multiple of the Kelvin wavelength (Hogg 1980; Jordi et al. 2009; Mihanović et al. 2014; Igeta et al. 2015). Jordi et al. (2009) reported that wind-induced, island-trapped internal waves generated strong currents (reaching $1\,\mathrm{m\,s^{-1}}$) leading to sediment resuspension. In addition to wind stresses, diurnal tides (e.g., K_1 or O_1) are also a source of Kelvin-trapped waves (Kitade and Matsuyama 1997; Tanaka et al. 2010).

Oceanic tides are mainly forced by the superposition of the semidiurnal (S_2 and M_2) and diurnal constituents (K_1 and O_1). Because the semidiurnal tidal component is dominant in most coastal oceans, most studies of internal tides focused on the interaction of the barotropic semidiurnal tides with topography at midlatitudes (e.g., Wunsch 1975; Morozov 1995; Cacchione et al. 2002). However, despite the existence of the diurnal tidal constituent in much of the world's coasts, generation processes of diurnal internal tides at midlatitudes have not been given as much attention.

In this study, we conducted numerical simulations to investigate the generation mechanism of internal tides around Izu-Oshima Island located along the Izu–Ogasawara Ridge off Sagami Bay, Japan (Fig. 1). Kitdate and Matsuyama (1997) studied the propagation of internal tides in this area using a simplified two-layer model. They found that diurnal internal tides are trapped around the island. However, the simplified two-layer model did not reproduce the details of internal tide generation. In this paper, we demonstrate internal tidal generation processes associated with both semidiurnal and diurnal tidal constituents using the three-dimensional Stanford Unstructured Nonhydrostatic Terrain-following Adaptive Navier–Stokes Simulator (SUNTANS) (Fringer et al. 2006). We follow the approach of Kang and Fringer (2012), who studied the internal tide generation processes in Monterey Bay, California, using SUNTANS.

Physical processes around Izu-Oshima Island from field observations are described in section 2. The model setup and model validation are presented in section 3. Section 4 presents generation processes and energetics of internal tides. Section 5 summarizes this study with major conclusions.

2. Observations of internal tides around Izu-Oshima Island

Izu-Oshima Island is located along the Izu–Ogasawara Ridge off Sagami bay, Japan (Fig. 1). The Izu–Ogasawara Ridge extends from approximately 600 km south of Japan to the Sagami Bay region (Fig. 1a). The barotropic tides
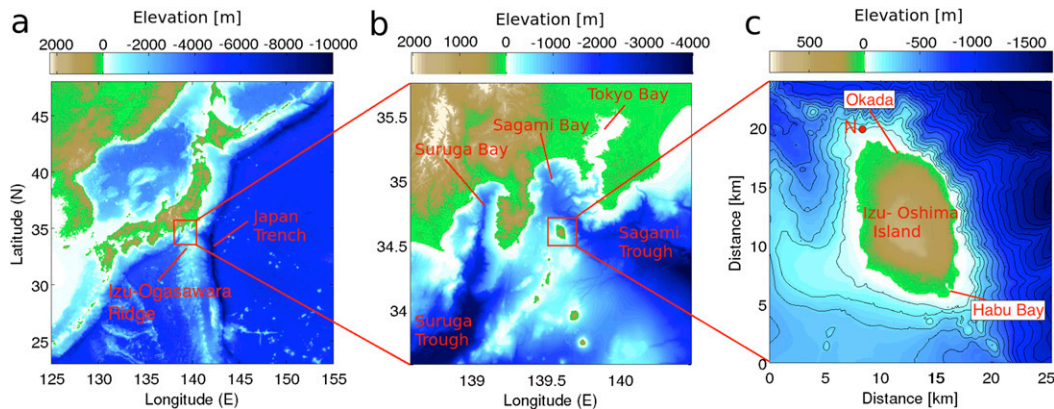
FIG. 1. Bathymetry around the Japan mainland and Izu-Oshima Island. Data from location N on the north side of the island is shown in Fig. 8. The tidal gauge station Okada is described in section 3e, while the OCEANS underwater observatory is located in Habu Bay.

propagate across this ridge from east to west and generate strong tidal currents (Ohwaki et al. 1991). A chain of islands is located along the ridge, of which Izu-Oshima is the largest and farthest to the north. The island is approximately elliptical and is 15 km long with a circumference of roughly 52 km, and its ellipticity is roughly 0.8 (Fig. 1c). Izu-Oshima Island is located between the Sagami Trough and the Suruga Trough (Fig. 1b). The Sagami Trough creates steep topography off the eastern coast of the island with slopes as large as 15°. The topography between the island and the Suruga Trough is gentler, and slopes do not exceed 2°.

The Oshima Coastal Environmental Data Acquisition Network System (OCEANS) is an underwater cabled observatory that was installed at a depth of 23 m on 13 August 2014 at the mouth of Habu Harbor at the southern tip of Izu-Oshima Island (Fig. 1c). This monitoring system is a real-time ocean environmental monitoring system and consists of a thermistor chain, an acoustic Doppler current profiler (ADCP), a plankton camera system [Continuous Plankton Imaging and Classification Sensor (CPICS)], a nitrate sensor, a fluorescence sensor, and a pressure sensor. There were 20 thermistor sensors mounted on the thermistor chain at intervals of 1 m from the bottom. Nitrate, fluorescence, and pressure sensors were mounted on the bottom of the mooring site. The sampling frequency for all sensors is 1 s. Because the ADCP was in preparations for survey during summer 2014, we could only compare model results to temperature data from the thermistor array for model validation in this paper.

Figure 2 shows an example of data from the OCEANS observatory in August 2014. In the dataset, the temperature time series show two regimes:

1) higher-frequency (roughly one-half day) temperature fluctuations associated with semidiurnal tides appeared at the beginning of the record (Figs. 2a,b; 13–19 August) and 2) strong and diurnal temperature fluctuations associated with diurnal tides (Figs. 2a,b; 19–23 August). In addition, both nitrate and chlorophyll a concentrations are high in the low temperature water mass (Figs. 2c,d). It is well known that internal tides lead to heaving of the cold layer on a shallow slope, as shown in Fig. 2. We assume that the appearance of cold-water intrusions is due to internal tides propagating into the study region. Although the temperature fluctuations associated with tidal frequencies were due to internal tides, the internal tidal phase was variable and not related to that of the sea surface height. The isothermal displacement exceeded 16 m (the length of the thermistor chain) at a depth of 23 m. The observed diurnal temperature fluctuations in Fig. 2 are likely the signature of island-trapped diurnal internal tides as initially reported by Kitade and Matsuyama (1997). In this study, we focus on the generation mechanism of the diurnal trapped waves around the island as well as semidiurnal internal tides.

Using the T-TIDE package (Pawlowicz et al. 2002), the amplitudes of the first four tidal constituents (M_2, S_2, K_1, and O_1) were 0.17, 0.37, 0.19, and 0.15 m, respectively, at the Okada tidal gauge station (Fig. 1c; located on the north side of Izu-Oshima Island) in August 2014. Although the amplitude of the diurnal constituents is less than the maximum of the semidiurnal constituents, the peak diurnal amplitude (e.g., $K_1 + O_1$) can be larger than the semidiurnal amplitude (e.g., $S_2 + M_2$) during semidiurnal neap tides. To evaluate the amplitude of the diurnal tides ($K_1 + O_1$) relative to the semidiurnal tides ($S_2 + M_2$), we estimated the form number (Pond and Pickard 1983), or the ratio
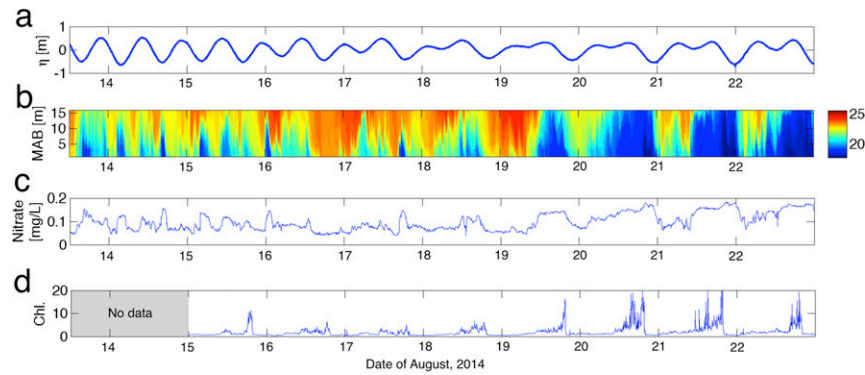
FIG. 2. Observations from the OCEANS observatory system: (a) tidal elevation, (b) temperature [°C; meters above the bottom (MAB)], (c) nitrate concentration, and (d) chlorophyll concentration (μg L^{-1}). Nitrate and chlorophyll data were collected at the bottom of the mooring system (depth = 23 m).

of the diurnal tidal amplitude to semidiurnal tidal amplitude, given by

$$F = \frac{\eta_{\text{K1+O1}}}{\eta_{\text{M2+S2}}}, \qquad (3)$$

where $\eta_{\text{K1+O1}}$ ($\eta_{\text{M2+S1}}$) is the diurnal (semidiurnal) tidal range due to the superposition of the K$_1$ and O$_1$ (M$_2$ and S$_2$) tides. The form number varies over time due to phasing between the diurnal and semidiurnal spring tidal cycles (Fig. 3d). Although the amplitude of the diurnal constituents is less than the maximum of the semidiurnal constituents, the peak diurnal amplitude (e.g., K$_1$ + O$_1$) can be larger than the semidiurnal amplitude (e.g., S$_2$ + M$_2$) during semidiurnal neap tides. The time series of the form number shows two periods in which $F > 1$, namely, between 3–8 and 18–22 August 2014, with a maximum of $F = 1.5$ on 6 and 19 August (Fig. 3d). These time periods coincided with the periods in which the diurnal internal tides were strongest (Figs. 2, 3).
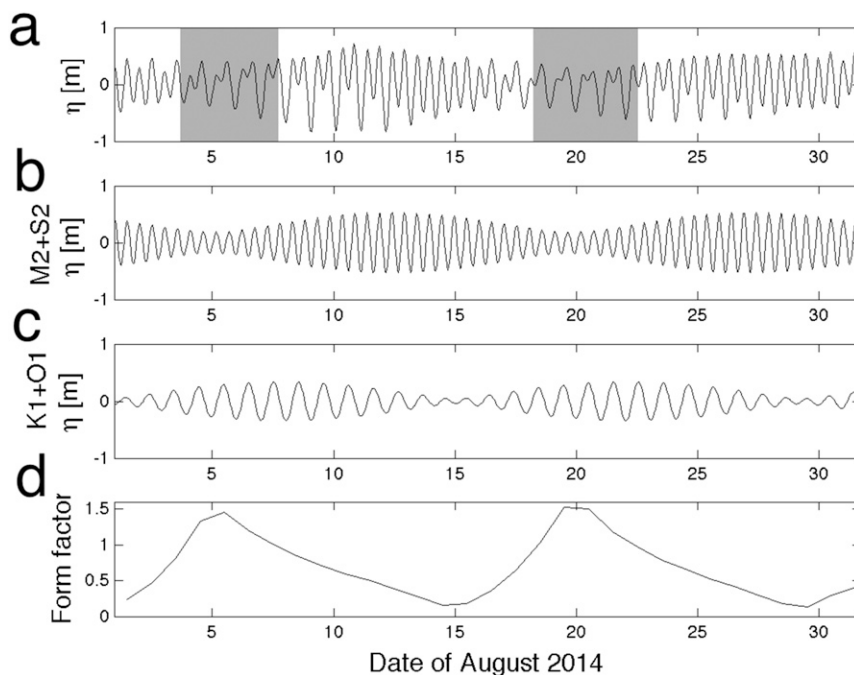

FIG. 3. Sea surface elevation at Okada tidal gauge station in August 2014: (a) observed tidal elevation, (b) semidiurnal tidal elevation (S$_2$ and M$_2$), (c) diurnal tidal elevation (K$_1$ and O$_1$), and (d) the form factor. Gray shaded periods in (a) indicate periods when the form factor exceeds 1.

3. Method

a. Model setup

We employed the hydrostatic version of SUNTANS (Fringer et al. 2006) to simulate internal tide generation processes around Izu-Oshima Island. SUNTANS solves the three-dimensional, Reynolds-averaged, Navier–Stokes equations with the Boussinesq approximation, along with the continuity equation, the depth-averaged continuity equation, and transport equations for salinity and temperature. The density is computed from the temperature, salinity, and pressure using the equation of state from Millero and Poisson (1981). In this study, no turbulence model is used and horizontal diffusion of scalars is set to zero. For momentum, the horizontal eddy viscosity ν_H and the vertical eddy viscosity ν_V are set to 1 and 5×10^{-3} $m^2\,s^{-1}$, respectively. The bottom drag coefficient is constant and given by $C_D = 0.0025$, and a constant Coriolis frequency of 8.4×10^{-5} rad s^{-1} is specified (at latitude of 35°N). A time step of $\Delta t = 30\,s$ is used, dictated by the stability of explicitly computed internal gravity waves. Because we focus on internal tides generated by the barotropic tides, no surface heat flux or winds are imposed. For further model details, refer to Kang and Fringer (2012).

b. Bathymetry and grid

To avoid reflecting internal tides from the model boundaries, the domain is expanded by approximately 1500 km in the x direction (east–west) and 800 km in the y direction (north–south), with the largest horizontal grid spacing of 50 km horizontally near the boundaries (Fig. 4). As they do not impact the baroclinic tides in the study region, simplified coastline and bathymetry are assumed in the expanded region. The horizontal grid spacing is compressed to 3 km at the edges of the 200 km × 200 km study region and is further refined near Izu-Oshima Island to 100 m (Fig. 4c). In the vertical, there are 100 z levels with refinement near the sea surface; the minimum and maximum vertical grid cell sizes are 2.4 and 117 m, respectively. Although there are seven islands in the region, the model only resolves Izu-Oshima, Nijima, Kozu, and Miyake Islands (Fig. 4b), while the other islands are not resolved owing to grid resolution constraints (they do not impact the results of interest). The Japan Trench runs along the eastern boundary of Japan with depths as large as 10 000 m (Fig. 1a). Although this trench affects large-scale global ocean circulation and heat fluxes, baroclinic internal tides are generated in waters shallower than 3000 m (Kang and Fringer 2012). According to a global ocean circulation model, most internal tidal energy conversion and dissipation occur in depths shallower than 3000 m (Buijsman et al. 2016). Therefore, the maximum depth of the model is set to 3000 m to reduce the computational effort associated with resolving the deep trench. As a result, the depth is assumed to be uniform at 3000 m outside the region of interest.

c. Initial condition

Initial temperature and salinity were taken from the *World Ocean Atlas 2009 (WOA09;* National Oceanographic Data Center) data archives and were assumed to be horizontally uniform. We selected summer seasonal climatic data in the study area (Fig. 5). As shown in Fig. 5b, the salinity minimum layer appears at a depth of 700 m, which is formed by an intrusion of cold and low-salinity Oyashio water from the north. The initial velocity and free surface were set to zero throughout the numerical domain. Because the climatic data from *WOA* were obtained from averages over numerous observed datasets, the *WOA* data are not sufficient to reproduce the local stratification needed to model the observed results in Fig. 2. Therefore, we created a modified initial temperature field for the specific period of August 2014 with the following assumptions:

1) Temperature is 24.5°C between 0- and 20-m depth.
2) The temperature gradient between 20- and 35-m depth is taken from observed stratification from the OCEANS observatory, shown in Fig. 5c as a red line.
3) Temperature below 200 m is taken from *WOA* seasonal climatic data.
4) Temperature between 35- and 200-m depth is interpolated from the upper (above 30 m) and lower (below 200 m) temperature data with cubic spline interpolation.

The modified initial temperature profile is shown in Fig. 5c. To validate the model performance within the specific period shown in Fig. 2 (13–23 August 2014), model runs designed to reproduce observations from the OCEANS observatory were initialized with this modified temperature field. The original *WOA* temperature and salinity initial conditions were used to investigate general internal tidal dynamics during the summer season. In what follows, we refer to these as modified *WOA* or *WOA* initial conditions.

d. Tidal forcing

Because the model bathymetry is simplified near the ocean boundaries with a constant depth of 3000 m, we did not use predicted tides from a global tidal model [e.g., Oregon State University (OSU) Tidal Inversion Software (OTIS); Egbert and Erofeeva 2002]. Instead, we assumed that barotropic tides propagate from east to west in the domain with tidal currents parallel to the southern boundary of the domain. Such behavior of the semidiurnal and diurnal barotropic tides is well documented along the southern coast of mainland Japan (Ohwaki 1991; Le Provost et al. 1994). Under this assumption, the
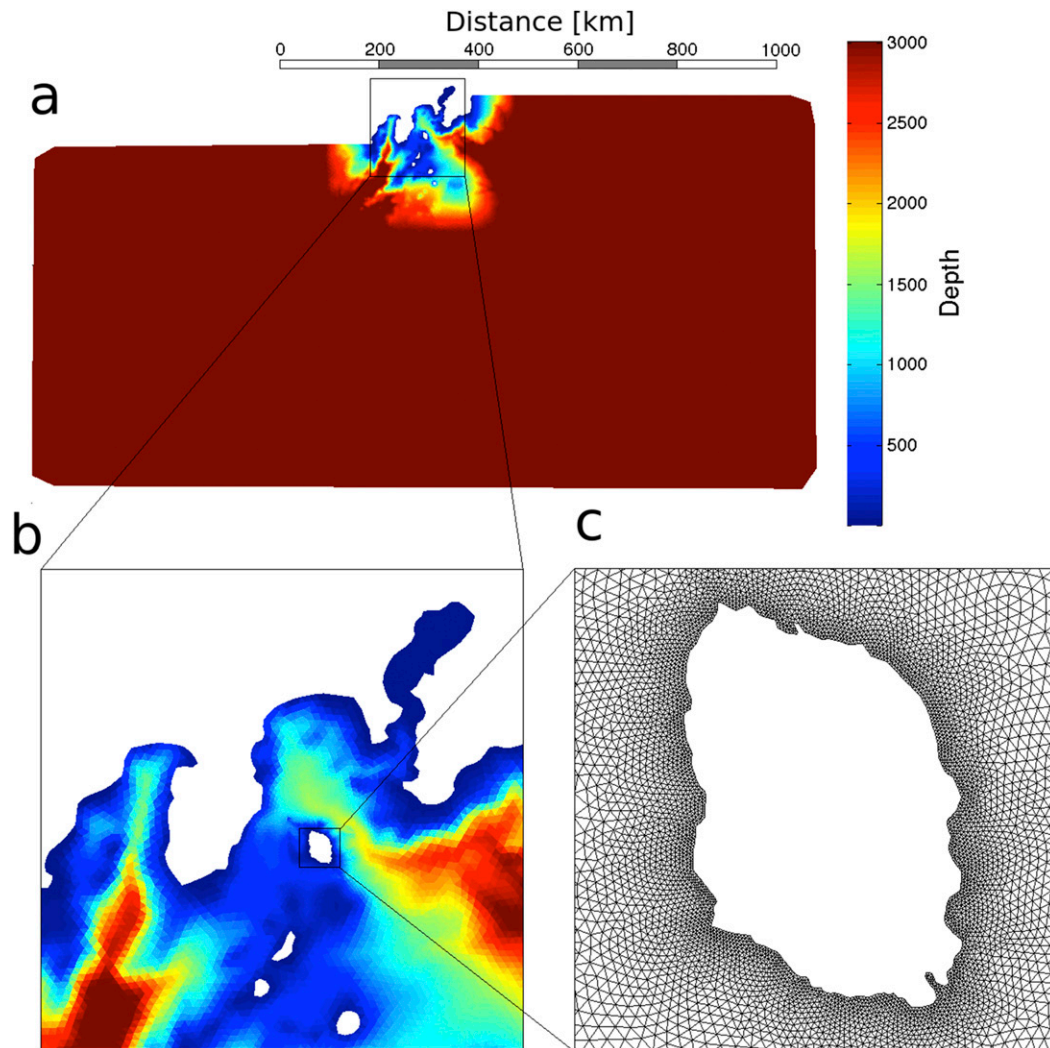
FIG. 4. (a),(b) Bathymetry (m) of the model domain and (c) a magnified view showing the grid around Izu-Oshima Island. From north to south, the islands in (b) are Izu-Oshima, Nijima, Kozushima and Miyake.

eastern and western boundaries of the domain were forced with an east–west barotropic velocity of the form

$$u_b = \sum_i^{N_t} A_i \cos[k_i x - \omega_i(t + \lambda_i)], \qquad (4)$$

where A_i is the velocity amplitude, k_i is the wavenumber, x is the horizontal distance in the east–west direction, t is the time, λ_i is the phase lag, and the subscript i indicates the tidal constituent. The southern boundary was assumed to be a free-slip boundary along which the flow is assumed to be parallel. To reproduce tidal elevations caused by the velocity boundary forcing, we estimated the velocity amplitude A_i using linear wave theory with

$$A_i = a_i \sqrt{\frac{g}{h}}, \qquad (5)$$

where a_i is the free-surface amplitude, and h is the depth at the boundaries. In this study, the depth at all open boundaries was given by $h = 3000$ m. The velocity amplitude estimated with (5) is the velocity for producing tidal elevations at the deep boundary. To reproduce realistic tidal elevations around the island, the forcing amplitudes of the individual tidal constituents were computed with a Newton method, as outlined in the appendix. To minimize transient oscillations, the boundary velocities were spun up with

$$u_{b_{\text{actual}}} = u_b[1 - \exp(-t/\tau_r)], \qquad (6)$$

where $\tau_r = 1$ day. We also employed a sponge boundary layer at the eastern, western, and southern boundaries to prevent boundary reflections of internal waves (Zhang et al. 2011; Kang and Fringer 2012). In addition to
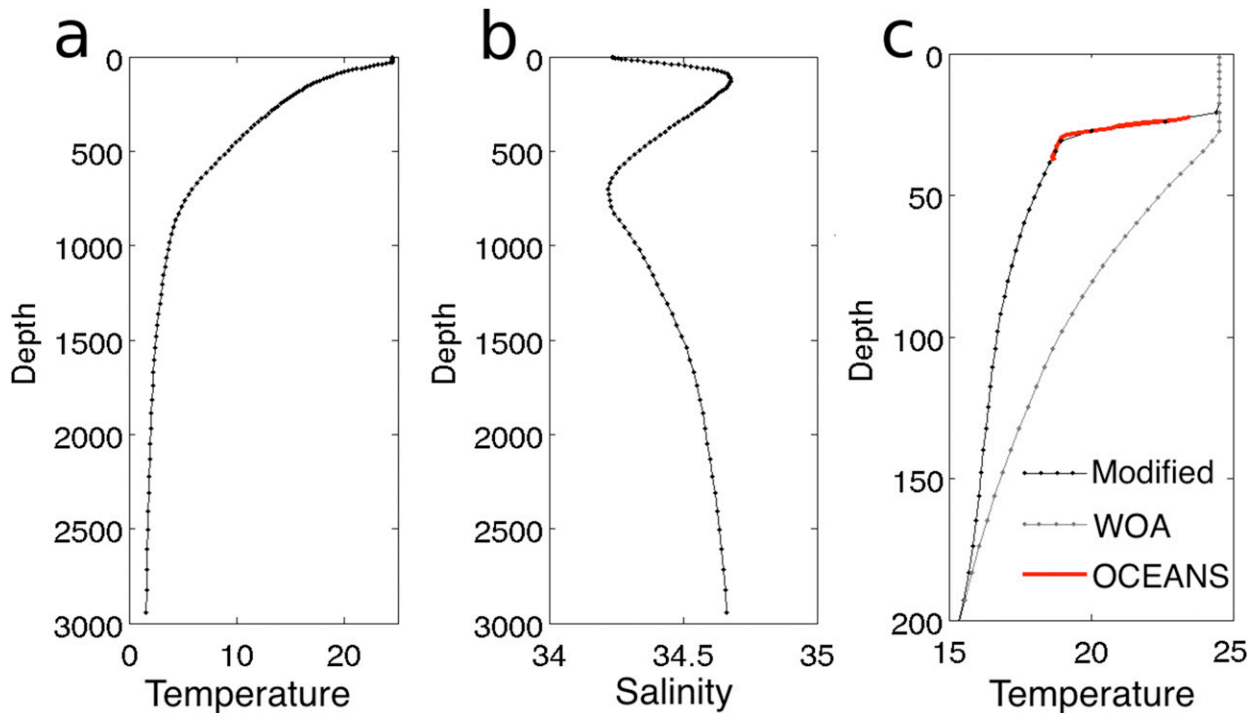
FIG. 5. Initial conditions for (a),(c) temperature (°C) and (b) salinity (psu). The dots represent points on the *z*-level grid.

realistic tidal conditions, to investigate physical processes induced by the diurnal and semidiurnal tides, we also conducted simulations with one tidal constituent, namely, the M_2 (semidiurnal) or K_1 (diurnal) tidal frequencies, both with a tidal elevation of 0.5 m. In this study, we focus on model results from three runs summarized in Table 1. We also conducted an additional 11 model runs under variable forcing frequencies (1/44–1/16 cph) for a frequency response analysis (see section 4b).

e. Model validation

Predicted tidal elevations from run 1 were compared to observed tidal elevations obtained at the Okada tide gauge station [Japan Metrological Agency (JMA)] located on the north side of Oshima Island (Fig. 6). To validate the model surface elevations, we computed the model skill score (Murphy 1988) as

$$\text{Skill} = 1 - \frac{\sum (\eta_O - \eta_M)^2}{\sum (\eta_O - \overline{\eta_O})^2}, \quad (7)$$

where η_O is the observed tidal elevation, η_M is the modeled tidal elevation, and the overbar denotes the time average. The time average and the summation were computed using data at 1-h intervals during the last 16 days of the 20-day simulation. The model skill score

for surface elevations from run 1 was 0.97. The root-mean-square error (RMSE) and the correlation coefficient between observed and modeled tidal elevations were 5.2×10^{-2} m and 0.99, respectively. The centimeter-scale RMSE is due to tidal constituents not included in the model. We also compared amplitudes and phases of each tidal constituent from run 1 to the observed tidal elevation. The RMSE of each tidal constituent E and the relative RMSE R_E are defined as

$$E = \sqrt{\frac{1}{2} \left(a_O^2 + a_M^2 \right) - a_O a_M \cos(G_O - G_M)}, \quad \text{and} \quad (8)$$

$$R_E = \frac{E}{a_O}, \quad (9)$$

TABLE 1. Initial and boundary conditions for the model runs conducted in this paper. *WOA* is the initial condition taken from summer season climate data provided by the *World Ocean Atlas*. Modified *WOA* is the initial condition composed of data from both *WOA* and OCEANS observations for model validation (section 3e).

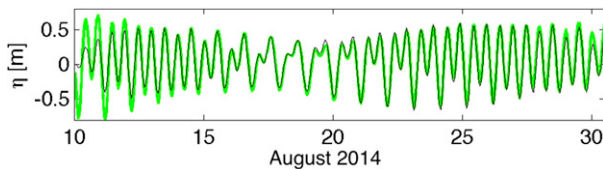|	Run 1	Run 2	Run 3
Tide	S_2, M_2, K_1, O_1	K_1	M_2
Initial condition	Modified *WOA*	*WOA*	*WOA*
Period	10–30 Aug 2014	20 tidal periods	20 tidal periods

FIG. 6. Tidal elevations from run 1 (thin light green line) and observations (thick gray line) at the Okada tide gauge station.

TABLE 2. RMSE (m) and the relative RMSE (%) for each tidal constituent.

	S_2	M_2	K_1	O_1
E	1.8×10^{-4}	8.9×10^{-4}	1.7×10^{-3}	2.1×10^{-3}
R_E	0.082	0.247	0.973	1.514

(Carter 2010; Kang and Fringer 2012), where G is the phase and subscripts O and M denote observations and predictions by the model, respectively. The terms E and R_E for each tidal constituent are shown in Table 2. Estimated relative errors for all four tidal constituents are of the order of 1% or 0.1%, which indicates good agreement between modeled and observed tidal elevations. The average value of the relative error for all constituents was 0.704%.

In addition to tidal elevations, we also compared temperature fluctuations due to internal tides between simulations and observations. When diurnal tides were dominant, the temperature fluctuations were reproduced by the model (Fig. 7, especially during 20–23 August). Observed data showed high-frequency (frequency much higher than tidal frequencies) motion likely induced by nonlinear processes that are not computed in the model due to the limited resolution, which would need to be O (10) m, following Vitousek and Fringer (2011). To compare observed to simulated data without such high-frequency fluctuations, simulated bottom temperature data were filtered using a bandpass filter with a frequency between 9.26×10^{-5} and $9.26 \times 10^{-6} \, \mathrm{s}^{-1}$ (period between 3 and 30 h). Bandpass filtered bottom temperature from the model showed good agreement with the observed data when the diurnal tides were dominant (Fig. 7d; 20–23 August). The skill score was estimated with the same method as the validation for tidal elevations [(7)] and was 0.63 between 20 and 23 August for bottom temperature. According to Allen et al. (2007), a skill score of 0.63 is designated as "very good." The correlation coefficient between simulated and observed data for the same time period was 0.84, which implies that the phase of internal tides from the model matches the observed results. Although the amplitude of the internal tides was underestimated in the model likely due to unresolved nonlinear processes, the vertical structure and phasing of the internal tides were reproduced by the model (Figs. 7e,f). The underprediction of the diurnal motions may also arise from a lack of wind forcing in the model because diurnal winds are ubiquitous in coastal oceans (e.g., Gille et al. 2003) and can generate island-trapped internal waves (Jordi et al. 2009; Mihanović et al. 2014).

In contrast to the diurnal internal tides, the results from run 1 showed intermittent internal bores when semidiurnal tides were dominant (13–18 August), although this was not consistent with observed data. The skill score and correlation for the bottom temperature were 0.054 and 0.128, respectively, when semidiurnal tides were dominant (13–18 August). The semidiurnal internal tides were not accurately predicted by the model because they are generated remotely where the grid resolution was not sufficient to resolve the generation. Furthermore, the semidiurnal internal tides are generated far away and so propagate over long distances through a stratification that is not realistic since it is initially homogeneous in the horizontal. Over long propagation distances, the semidiurnal internal tides are also modulated by background flows (e.g., Rainville and Pinkel 2006).

4. Results and discussion

a. Internal tides generated around Izu-Oshima Island

As shown in Fig. 8, the amplitude of isothermal displacements from run 1 reached 25 m on the north side of the island on 20 August. Strong currents were generated by the diurnal tides with a maximum speed of $0.65 \, \mathrm{m \, s}^{-1}$ (Figs. 8c,d). Thus, the diurnal internal tides dominated the internal wave field in the vicinity of the island. Although features of the internal tide at other locations around the island showed similar structure, semidiurnal internal tides on the eastern boundary were weaker than they were at other locations, and diurnal internal tides on the southern boundary were weaker than they were at the other locations.

b. Island-trapped internal waves

To focus on the diurnal internal tides, we ran the model with only diurnal tidal forcing (K_1 tidal frequency; run 2). Simulated results from this run clearly showed island-trapped internal waves around Izu-Oshima Island with the first azimuthal mode (Fig. 9). Generally, the first internal wave mode dominates in shallow regions (Halpern 1971), and the displacement of the main thermocline (or the maximum density gradient layer) is representative of the amplitude of the internal tide. However, in deeper water where higher
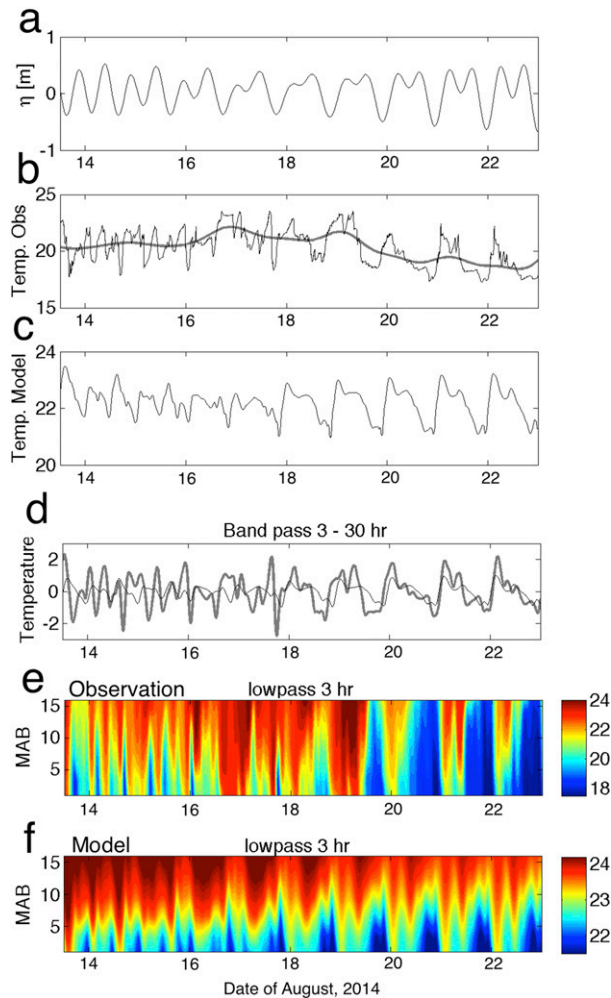
FIG. 7. Comparison between observed and modeled results from run 1: (a) modeled tidal elevations, (b) bottom temperature (°C) from the OCEANS observatory, (c) bottom temperature from the model at the OCEANS observatory, (d) bandpassed filtered (1/30–1/3 cph) bottom temperature during the diurnal internal tide period for the observation (thick gray line) and the model (thin black line), and low-pass filtered (1/3 cph) vertical temperature time series from (e) the observation and (f) the model. The thick line in (b) is the background, low-frequency temperature signal at frequencies lower than 1/30 cph.

FIG. 8. Model results from run 1 for August 2014 at station N in Fig. 1c. Time series of (a) tidal elevation, (b) temperature (°C), (c) east–west velocity, and (d) north–south velocity on the north side of the island.

modes may be more important, the internal tide may lead to large displacements of a different isotherm, particularly in the presence of the deeper permanent thermocline. This is not necessarily the case for trapped waves, for which we expect the maximum displacement within the water column to correspond to the same isotherm within one internal Rossby deformation radius from the coast. This is corroborated by our results that indicate that the 21°C isotherm shows the largest isotherm displacement in the water column in both shallow and deep regions around the island.
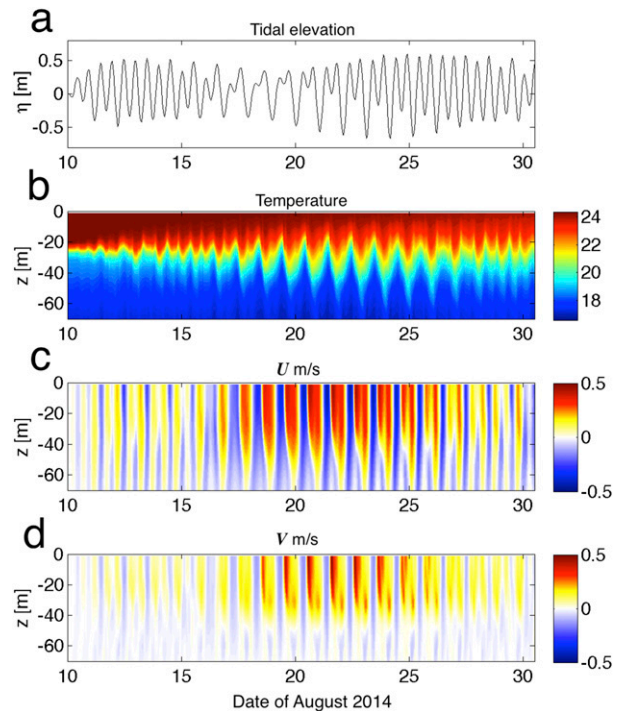
Therefore, the displacement of the 21°C was used as an indicator of the amplitude of the internal tides. Figure 9 shows the spatial distribution of the displacement of the 21°C isotherm (Fig. 9a) and time series of isothermal displacements along a circular transect 2500 m from the island coast (Fig. 9d). The amplitude of the 21°C isotherm displacement was estimated around the island using a harmonic analysis with the K_1 frequency (Figs. 9b,e). The diurnal internal tides propagate clockwise around the island, and the isothermal displacements increased toward the island coast (Figs. 9b,c), as is typical of coastal Kelvin-trapped waves (Longuet-Higgins 1969; Hogg 1980). A shallow ridge located on the west side enhanced the isothermal displacements around the island. The amplitude of the displacements exceeded 20 m on the northwest side of the island (Figs. 9b,e), which is 40 times larger than the surface elevation caused by barotropic tides. Moreover, on the south side, the isothermal displacements are much smaller (Figs. 9b,e).

Theoretical approaches for island-trapped waves have been developed in the literature, focusing on 1) trapped waves around a circular island with a flat bottom (Longuet-Higgins 1969; Hogg 1980) and 2) trapped waves around a circular island with topography (Brink 1999).
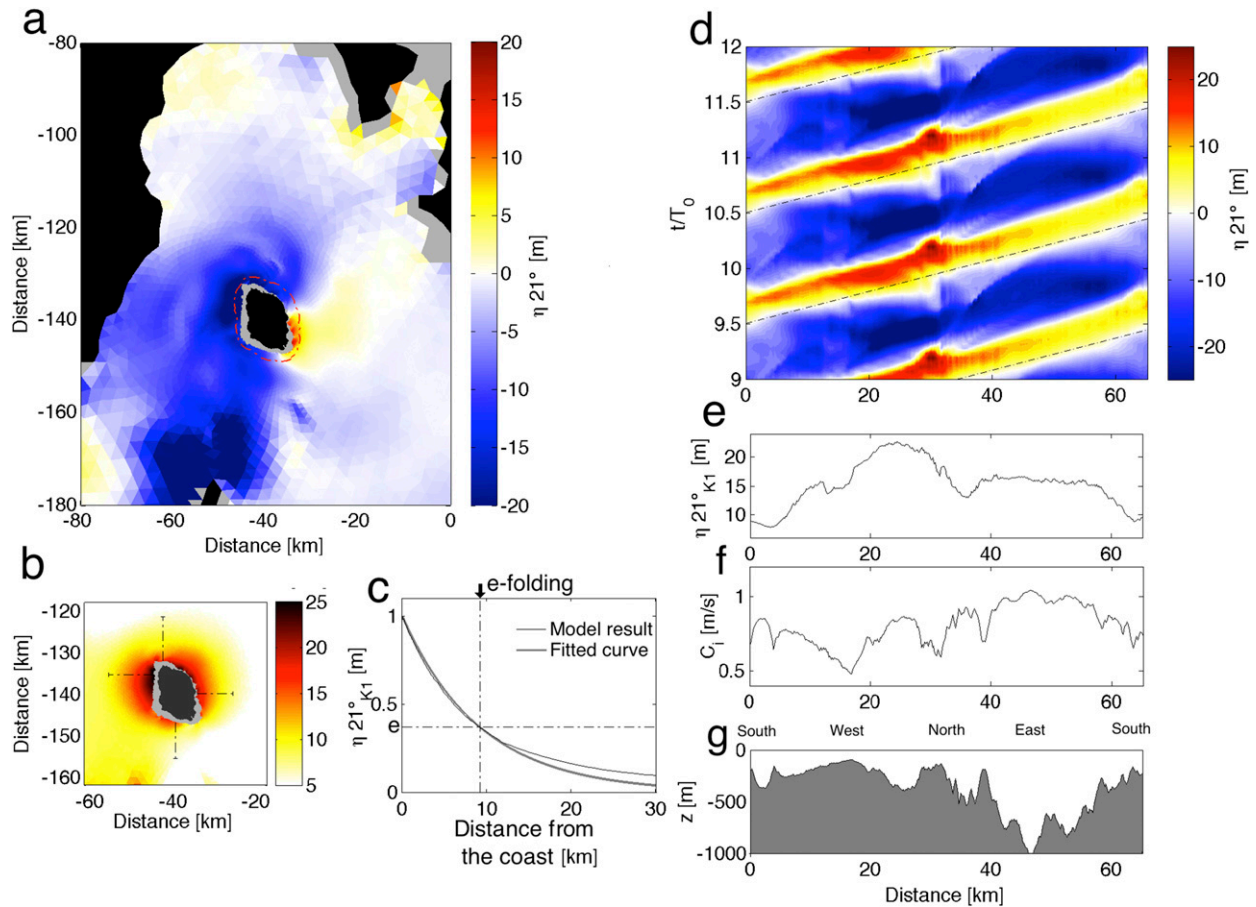
FIG. 9. Vertical displacement of the 21°C isotherm for the K_1 forcing case (run 2): (a) map of the isothermal displacement at $t = 252$ h ($t/T_0 = 10.5$; T_0 is the K_1 period), (b) amplitude of the isotherm displacement around the island, (c) amplitude of the isothermal displacement along the south–north transect shown in (b) as a black dashed line, (d) isothermal displacement as a function of t/T_0 along the transect around the island along with the bathymetry along this azimuthal transect in (g), (e) the amplitude of the isothermal displacement along the azimuthal transect, and (f) the first-mode internal wave phase speed estimated from the two-layer wave theory. The azimuthal transect in panels (d)–(f) is clockwise and 2.5 km from the coast of the island beginning on its southern end and is indicated as a red dashed line in (a). Black dashed lines in (c) show the average wave propagation speed of 0.84 m s^{-1}. The black dashed lines in (c) indicate the e-folding distance on the transect.

However, such theoretical methods are difficult to apply to the complicated bathymetry in our study region. Thus, by computing the internal wave travel time around the island, the critical wave frequency for resonance can be estimated with

$$\omega_C = 2\pi/T_C, \qquad (10)$$

where $T_C = c_i/L_C$ is the internal wave travel time around the island. Here, c_i is a representative internal wave speed, and L_C is the island circumference at a distance of 2.5 km from the coast, as shown in Fig. 9a. Strong resonance is likely to occur when the critical wave frequency is an integer multiple of the tidal frequency.

To estimate the first-mode internal wave propagation speed needed for the critical wave frequency, we employed two independent methods. Using two-layer

theory in which the two layers are delineated by the depth of maximum buoyancy frequency of the initial stratification, the first-mode internal wave propagation speed a distance of 2.5 km from the coast ranges from 0.48–1.04 m s^{-1}, with an average of 0.84 m s^{-1} (Fig. 9f). This agrees with model results from run 2 (Fig. 9d) and gives a critical frequency of $\omega_C = 8.09 \times 10^{-5}$ rad s^{-1}. Despite the variable depth around the island, the wave speed shown in Fig. 9d appears to be constant because the scale of the topographic variability is much shorter than the internal tidal wavelength. A second estimate of the internal wave speed was computed with the e-folding distance of the wave amplitude. Assuming Kelvin wave behavior, the internal wave speed can be estimated with

$$c_i = L_e f, \qquad (11)$$

where L_e is the *e*-folding distance over which the iso-therm displacement decays from the coast. This dis-tance was estimated to be 9.2, 10.9, 9.7, and 10.7 km on the eastern, western, southern, and northern sides of the island, respectively (see Fig. 9b), with an average of 10.2 km. An example of the normalized isotherm dis-placement plotted with a fitted curve of $\exp(-x/L_e)$ on the east side of the island is shown in Fig. 9c. Assuming $L_e = 10.2$ km gives $c_i = 0.85$ m s^{-1} and $\omega_C = 8.19 \times 10^{-5}$ rad s^{-1}. This wave speed is close to that derived from the two-layer theory and agrees with model results from run 2. The critical frequency from the two methods is close to the K$_1$ frequency (7.29×10^{-5} rad s^{-1}), which implies that the lowest (first) azimuthal mode related to island-trapped waves can exist and resonate with the diurnal tides.

To further quantify the resonance of island-trapped waves, we conducted a frequency response analysis using an additional 11 model runs under variable tidal forcing frequencies (1/44–1/16 cph; runs 4–14). All model parameters are the same as those for runs 2 and 3 except for the forcing frequency of the barotropic tide at the boundaries. Figure 10 shows the amplitude of the 21°C isotherm displacement on the north side of the island for runs 2–14 as a function of the forcing frequency and shows resonance at the diurnal K$_1$ frequency. The resonance can be quantified with the quality factor Q, which is a ratio of the center frequency (K$_1$ in this study) of the response curve to the width of the curve where the amplitude is half of the peak (Brink 1999). The quality factor is a measure of the damping of the system, with lower values implying stronger damping. Our results indicate a quality factor of $Q = 2.4$, which is lower than values reported in the literature (e.g., $Q = 6.8$, Mihanović et al. 2014; $Q = 8.2$, Caldwell and Eide 1976). Mihanović et al. (2014) re-ported that dissipation in their study was the cause of a lower Q value. Enhanced dissipation because of strongly variable topography and radiation of higher-frequency, nonlinear wave energy could be the source of the damping and small value of Q in our study. In the study by Mihanović et al. (2014), the maximum currents were approximately 0.2 m s^{-1}. In our study, the maximum currents around the island were much higher and reached 1.0 m s^{-1}, which may be a source of strong dis-sipation of internal wave energy leading to our relatively low value of Q. We note that these results were obtained with a summer stratification when the natural frequency is higher than it is during the winter when the stratifica-tion is weaker and the internal wave speed is lower. Therefore, diurnal resonance may not be as strong in the winter because of the lower resonant frequency or during
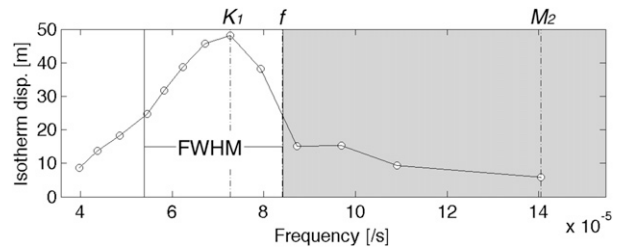

FIG. 10. The 21°C isotherm displacement as a function of the forcing frequency (s^{-1}) on the north side of the island (shown as N in Fig. 1). The gray shaded area indicates super inertial frequencies that propagate and do not resonate. FWHM is the half-width at half maximum.

times of the summer when the stratification is stronger than that employed here.

c. Energetics of internal waves

1) BAROCLINIC INTERNAL WAVE ENERGY FLUX

To investigate the source and energetics of diurnal and semidiurnal internal tides, we compute the depth-integrated baroclinic (BC) internal wave energy flux with the model results. The dominant BC energy flux is given by (Kang and Fringer 2012)

$$F_E = \int_{-d}^{\eta} p' \mathbf{u}'_H \, dz, \qquad (12)$$

where p_0 is the initial hydrostatic pressure or back-ground pressure field, $p' = p - p_0$ is the perturbation pressure, and $\mathbf{u}'_H$ is the horizontal baroclinic velocity vector $\mathbf{u}'_H = \mathbf{u}_H - \mathbf{U}_H$. Here, $\mathbf{U}_H$ is the horizontal baro-tropic velocity vector given by

$$\mathbf{U}_H = \frac{1}{H} \int_{-d}^{\eta} \mathbf{u}_H \, dz, \qquad (13)$$

where H is the total depth ($d + \eta$). The BC energy flux is computed using data from the last 10 tidal cycles of the simulations for the K$_1$ (run 2) and M$_2$ (run 3) forcing cases.

The BC energy flux for run 2 (K$_1$ forcing) showed clockwise fluxes around Izu-Oshima Island (Fig. 11a). Clockwise fluxes also appeared around the other islands resolved in the model. The flux reached 6 kW m^{-1} on the north side of Izu-Oshima Island, and it was weaker on the south side of the island, where it was diminished by opposite-signed flux by trapped waves around Nijima Island located to the south. In addition to the flux from island-trapped waves, strong BC wave energy fluxes reaching 10 kW m^{-1} appeared on the west side of the Izu Peninsula (east of Suruga Bay; Fig. 11a). Seamounts
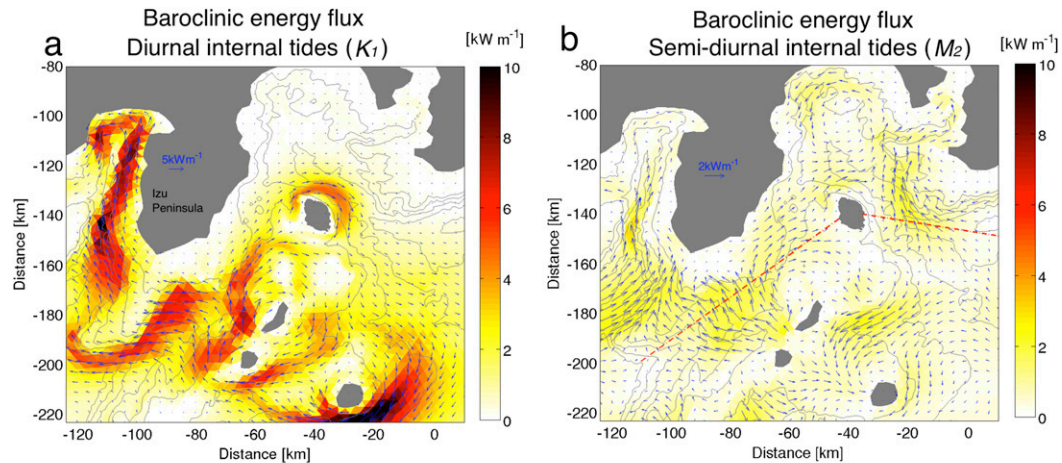
FIG. 11. BC energy flux for (a) the K_1 forcing case (run 2) and (b) the M_2 forcing case (run 3). Bathymetry contours in (a) and (b) are spaced at 500-, 1000-, 1500-, 2000-, 2500-, and 3000-m depths. Red dashed lines in (b) indicate transects for Fig. 12.

and ridges also support Kelvin-trapped internal waves. Ohwaki et al. (1991) reported that the Izu–Ogasawara Ridge contributes to enhanced Kelvin-trapped internal tides in Suruga Bay using a simplified two-layer model. They suggest that Kelvin-trapped internal tides propagate from far south to the bay, with an enhanced amplitude as they propagate into the bay because of topographic effects. Thus, internal tides were trapped on the west side of the Izu–Ogasawara Ridge, which results in high BC energy fluxes on the west side of Izu Peninsula.

The BC energy flux for the semidiurnal forcing case (run 3) was much weaker than that for the diurnal case (Fig. 11b). The intensity of the semidiurnal BC energy flux was similar to that in the case of Monterey Bay investigated by Kang and Fringer (2012), which is at a similar latitude and has similar barotropic tides. In contrast to the diurnal energy, semidiurnal internal wave energy is not trapped and propagates to Izu-Oshima Island from the west. The semidiurnal flux also appears on the eastern side of the island, although the energy flux was directed to the north and away from the island. Slope criticality was assessed by computing the slope of the internal wave beam for the M_2 tidal frequency from the dispersion relation [(1)], which indicates that the gentle slope to the west of Izu-Oshima Island was critical with respect to the M_2 internal tide (Fig. 12a) and leads to internal wave generation. Currents along a transect (oriented across the slope) show strong currents likely enhanced by the critical slope (Fig. 12a). On the other hand, the supercritical slope to the east was too steep to generate strong wave energy convergence on the slope (Fig. 12b). Instead, incident internal wave energy is reflected offshore.

2) BAROTROPIC–BAROCLINIC CONVERSION

In addition to BC internal wave energy flux, we estimated the barotropic–baroclinic (BT–BC) conversion rate, which indicates the conversion rate from BT tidal energy to BC tidal energy. The depth-integrated and time-averaged BT–BC conversion rate is defined as (Niwa and Hibiya 2004; Kang and Fringer 2012)

$$\langle \overline{C} \rangle = \langle \overline{\rho' g W} \rangle, \tag{14}$$

where overbars denote vertical integrals, brackets denote time average over a time interval T (10 tidal cycles in this study), and W is the barotropic vertical velocity given by

$$W = -\nabla_H \cdot [(d + z)\mathbf{U}_H]. \tag{15}$$

The depth-integrated and time-averaged BT–BC conversion rate is shown in Figs. 13a and 13b. Positive conversion rate implies generation of internal tides. A negative conversion rate can imply energy transfer from BC tides to BT tides, although it is more likely that negative conversion occurs because of the superposition of locally and remotely generated internal tides and is not an indicator of barotropic-to-baroclinic conversion (Zilberman et al. 2009; Kang and Fringer 2012). Strong conversion occurs around the islands and in Suruga Bay for the diurnal tidal forcing case (run 2; Fig. 13a). For the semidiurnal tidal forcing case (run 3), the conversion rate around the islands is much weaker than the diurnal tidal forcing case. However, the conversion rate at the mouth of Tokyo Bay and in Sagami Bay is slightly higher than the diurnal tidal forcing case. The strongest semidiurnal conversion rate occurs between Nijima
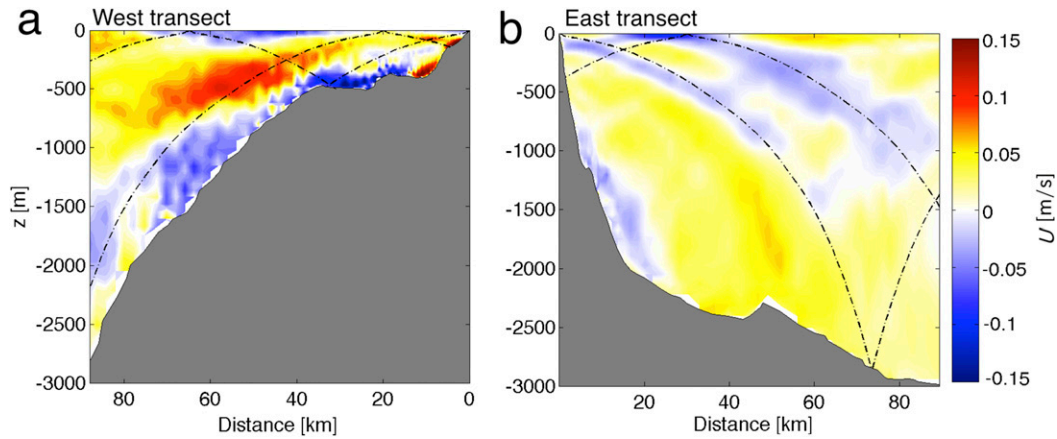
FIG. 12. Horizontal velocity parallel to the (a) west and (b) east transects indicated in Fig. 11 for run 4. Dashed lines show semidiurnal (M_2) internal wave beams estimated from the dispersion relation for superinertial internal waves [(1)].

Island and Kozu Island (Fig. 13b; at Easting −60 km and Northing −190 km), which is the same area as the large BC internal wave energy flux divergence (Fig. 11). Consequently, this area is a significant source of semidiurnal internal tidal energy in the study region.

The area-integrated conversion rate term in 150-m depth bins (Figs. 13c,d) and the cumulative fraction of conversion as a function of depth (the integrated area is the whole area shown in Figs. 13a,b) show that 66% of the diurnal conversion and 82% of the semidiurnal
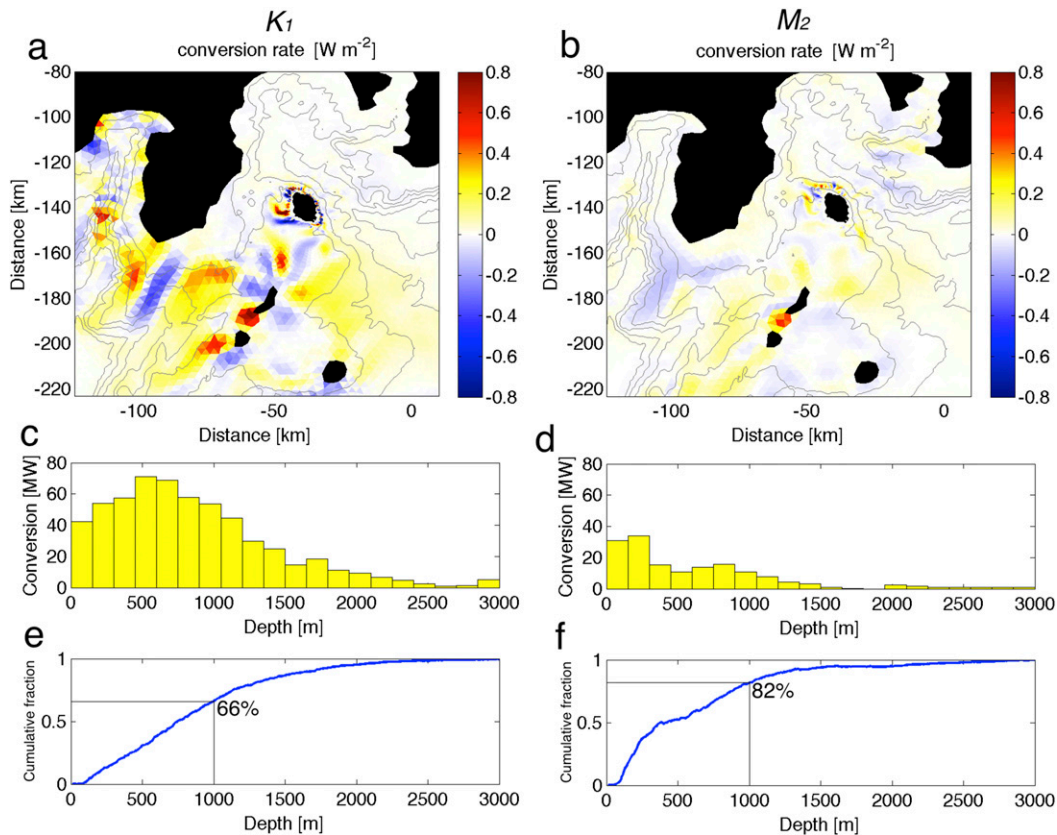

FIG. 13. Maps of the BT–BC conversion rate for the (a) K_1 (run 2) and (b) M_2 (run 3) frequencies, (c),(d) the area-integrated conversion in 150-m bins, and (e),(f) the cumulative fraction of the conversion rate.

conversion occur in shallow areas where the depth is less than 1000 m (Figs. 13c,d). Over 90% of the conversion occurs in depths less than 2000 m for both cases. The area-integrated conversion rate is 578 and 155 MW for the diurnal and semidiurnal forcing cases, respectively, in the area shown in Fig. 13. The conversion for the diurnal tides is approximately 2.4 times higher than that for the semidiurnal tides.

d. Tidal energy budget

The total energy budget is calculated by area integrating the period-averaged and depth-integrated energy terms following Kang and Fringer (2012):

Barotropic (BT) input: $-\sum \nabla_H \cdot \langle \overline{F_{E0}} \rangle \Delta A$, (16)

BT-BC conversion: $\sum \langle \overline{C} \rangle \Delta A$, (17)

BC radiation: $-\sum \nabla_H \cdot \langle \overline{F_E} \rangle \Delta A$, (18)

BT dissipation: $\sum (\nabla_H \cdot \langle \overline{F_{E0}} \rangle + \langle \overline{C} \rangle) \Delta A$, and (19)

BC dissipation: $\sum (\nabla_H \cdot \langle \overline{F_E} \rangle - \langle \overline{C} \rangle) \Delta A$, (20)

where Σ denotes summation over cells within a region, F_{E0} is the BT energy flux, and ΔA is the area of each grid cell. Values for these quantities can be found in Table 3. The dominant BT energy flux is given by

$$F_{E0} = \mathbf{U}_H H \rho_0 g \eta + \mathbf{U}_H \overline{p'}. \quad (21)$$

For more detail on the tidal energy budgets, refer to Kang and Fringer (2012). Each energy budget is calculated within 10 tidal cycles in a region shown in Fig. 14a (the region within the dashed lines). For the K_1 forcing case, 32% of the total BT input, or the energy flux convergence (1266 MW) is converted to internal tides, and 68% of BT input is dissipated in the region; 13% of the converted internal tidal energy is radiated away from the region. The M_2 forcing energy budget is approximately 2 times smaller than that of the K_1 forcing case. However, the percentage of the total BT input for each budget is almost the same for the K_1 (run 2) and M_2 (run 3) forcing cases.

For cases K_1 and M_2, 68% and 70%, respectively, of the BT input energy is dissipated as BT dissipation, which is approximately 6 times higher than the BT dissipation estimated in Monterey Bay, California, for M_2 forcing (Kang and Fringer 2012). This difference is likely due to the difference in the topography. In our study area, the barotropic tides propagate over the shallow Izu–Ogasawara Ridge, which incurs a drastic depth change from 3000 to 100 m over 50 km (Fig. 1). Therefore, large barotropic velocities over the shallow ridge may result in a large amount of BT dissipation in the study region.

TABLE 3. Tidal energy budget (MW) for K_1 and M_2 tidal constituents.

	K_1 (run 2)	M_2 (run 3)
BT input	1266 (100%)	738 (100%)
BT–BC conversion	405 (32%)	211 (29%)
BC radiation	160 (13%)	90 (12%)
BT dissipation	−861 (68%)	−528 (71%)
BC dissipation	−245 (19%)	−121 (16%)
Total dissipation	−1106 (87%)	−649 (88%)

e. High-frequency internal waves radiating from the island

High-frequency, small-scale internal wave motions have been frequently observed in coastal oceans (e.g., Farmer and Armi 1999; Moum et al. 2003; Kozlov et al. 2014). Farmer and Armi (1999) observed small-scale, solitary wave packets caused by tidal flows over a sill. Moum et al. (2003) observed high-frequency solitary waves propagating shoreward over the continental shelf. To investigate high-frequency and small-scale wave motions generated by tidal forcing, numerical results from run 2 (K_1 forcing case) were filtered using bandpass filters with frequencies of integer multiples of the K_1 frequency ω_{K1}. Bandpass filtered isothermal displacements show high-frequency harmonic internal waves generated around Izu-Oshima Island due to resonance with the K_1 barotropic tide (Fig. 15). The spectrum of the 21°C isotherm displacement on the north side of the island clearly shows frequency peaks at ω_{K1} harmonics with amplitudes that decay with increasing frequency. The isotherm displacements in Fig. 15 show that most of the energy in the higher harmonics is in phase with the low-frequency trapped wave motion, which implies that this high-frequency energy is trapped in the form of a weakly nonlinear Kelvin wave. However, some of the high-frequency waves propagate at speeds that are not consistent with the low-frequency motion, particularly on the northern and western portions of the island (Figs. 15d,e). The slower wave motion appears at frequencies of third and fourth harmonics with a phase speed of approximately 0.4 m s^{-1} (Figs. 15d,e). This phase speed is consistent with the second-mode wave on the west side of the island (distance 0–35 km along the transect). Indeed, the current structures on the northwest side show higher vertical mode motions in high-frequency bands (Figs. 15i–l). Therefore, we hypothesize that shoaling of the trapped wave over shallow topography produces nonlinear wave motions that produce both high-frequency and higher vertical mode waves. In addition, the characteristics appear to curve because they are advected by the strong, barotropic currents on the northern and western sides of the island (Fig. 15f).
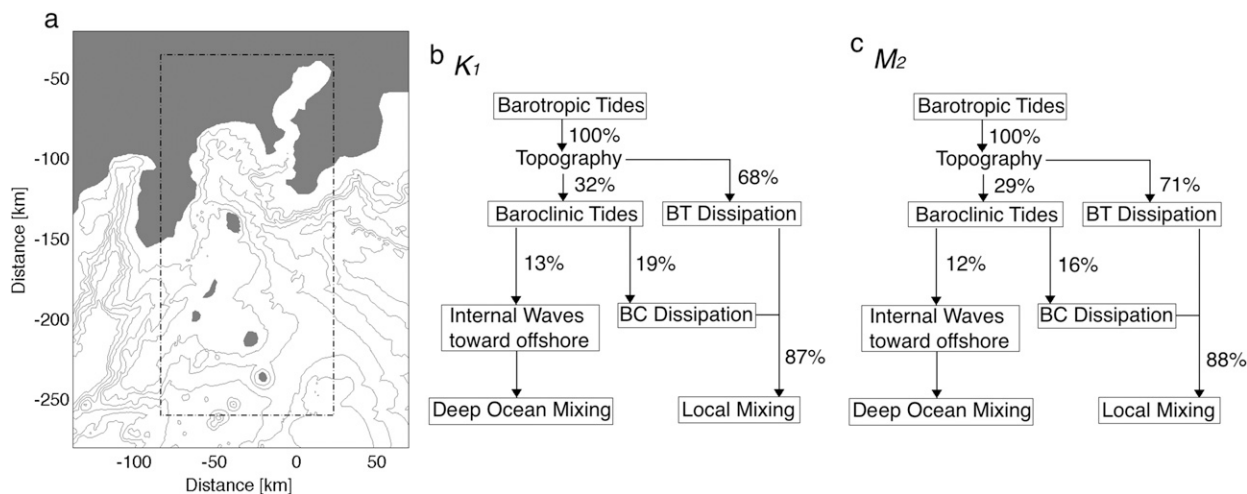
FIG. 14. (a) Region of the energy budget analysis and the energy budget schematics for the (b) K_1 and (c) M_2 tidal constituents from runs 2 and 3, respectively.

In addition to resonance with the diurnal barotropic tide, the high-frequency energy around the island can also arise from nonlinear hydraulics associated with the strong barotropic currents over the ridges that can generate small-scale, high-frequency lee waves (Bell 1975; Farmer and Armi 1999; Garrett and Kunze 2007). Because they arise from the interaction of the barotropic currents with topography, unlike those associated with resonance, nonlinear lee waves contribute to high-frequency motions that are not in phase with the trapped Kelvin wave. Hibiya (1986) reported that large values of the internal Froude number indicate the potential for enhanced lee-wave generation. Assuming first-mode internal waves, the Froude number is given approximately by $Fr = U/c_i = U/\sqrt{(N_{max}D/\pi)^2 + (f/k)^2}$ (e.g., Kundu 1990), where U is the barotropic flow speed, D is the water depth, and N_{max} is the maximum buoyancy frequency. The horizontal wavenumber k is assumed to be $2\pi/(1 \times 10^4)$ rad m^{-1} (the wavelength is assumed to be the length of the island ~10 km). Strong currents exceeding 1 m s^{-1} and regions with high Froude number exist around the island (Fig. 16a). However, we would expect regions in which $Fr > 1$ to be most dominant when they exist over large cross-shore scales, and hence nonlinear lee-wave effects are likely most pronounced over the western and northern ridges, which have the largest cross-shore extent of $Fr > 1$ (Fig. 16a). In high Froude number regions, lee waves are a potential source of the high-frequency motions that are not in phase with the trapped wave (Figs. 15, 16). Although the Froude number is quite high (Fr ~ 10) near the coast where the depth is shallower than the main thermocline, these nonlinear

dynamics do not affect the larger-scale energetics, owing to the relatively small amount of baroclinic energy in such shallow waters.

To quantify the fraction of high-frequency energy that radiates from the island, the BC internal wave energy flux was estimated for the high- and low-frequency components with a cutoff frequency of $3\omega_{K1}$ (Fig. 16). The intensity of the high-frequency internal wave energy flux is roughly 100 times less than that of the diurnal island-trapped internal tides (Fig. 16). Although small, the high-frequency fluxes provide insight into the fate of the high-frequency energy, which appears to radiate offshore on the western and northern sides of the island (Fig. 16a), while the low-frequency energy flux is predominantly parallel to the coast (Fig. 16b). The offshore flux of high-frequency energy to the south is likely a result of aliasing due to the interaction of energy propagating to this point from islands to the south (Fig. 16a). Although these results imply that high-frequency internal wave energy radiates from the island, the source of this energy is not clear (resonance and shoaling or lee-wave generation).

5. Conclusions

This study demonstrates generation of internal tides around Izu-Oshima Island, Japan, using SUNTANS validated with observations from the OCEANS. Although the model accurately predicts the diurnal internal tides, it is less accurate for the semidiurnal internal tides because these are remotely generated in regions of the domain where the grid
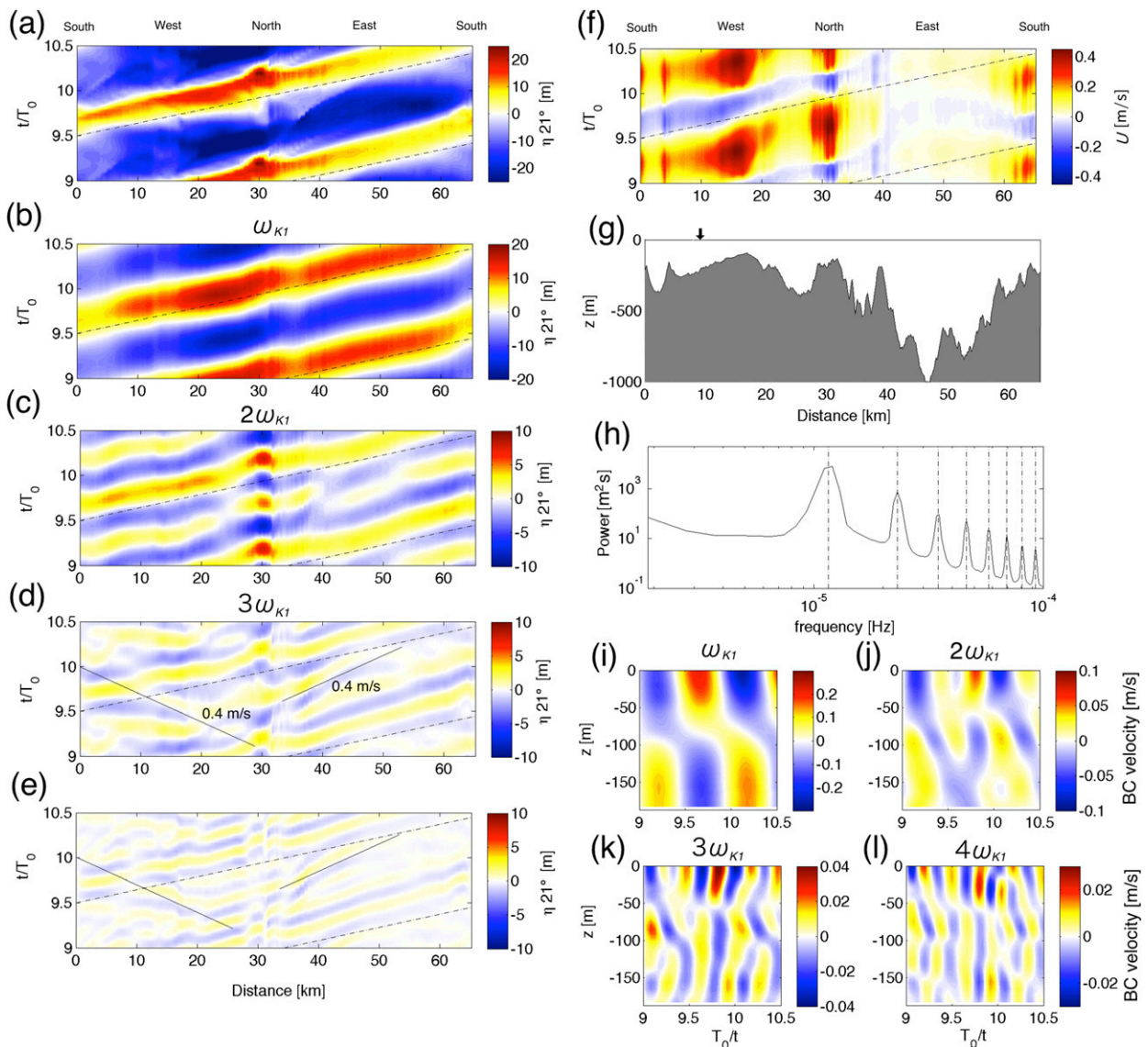
FIG. 15. Bandpass filtered vertical displacement of the 21°C isotherm along the azimuthal transect shown in Fig. 9a: (a) no filter; filtered with $n\omega_{K1}$, where n = (b) 1, (c) 2, (d) 3, and (e) 4; (f) barotropic flow speed oriented along the transect; (g) bathymetry along the transect; (h) spectrum of the displacement of the 21°C isotherm on the north side of the island (distance = 30 km); and (i)–(l) bandpass filtered alongshore baroclinic current speed on the northwest side of the island [distance = 10 km, indicated as a black arrow in the (g)]. Black dashed slope lines in (a)–(f) indicate the phase speed of $0.84 \, \mathrm{m \, s^{-1}}$. Black lines in (d) and (e) show the phase speed of $0.4 \, \mathrm{m \, s^{-1}}$. Vertical black dashed lines in (h) indicate frequencies at integer multiples of the K_1 frequency.

resolution could not be refined due to computational constraints. Resonance with the diurnal barotropic tides produces large-amplitude trapped internal tides that propagate in a clockwise direction around the island. This is the source of significantly more internal tide energy flux when the model is forced with the diurnal tide than when forced by the semidiurnal tide, as indicated by a BT–BC conversion rate that is twice as large for the diurnal case. Resonance of the trapped diurnal internal tides generates higher-frequency

harmonics that are in phase with the trapped wave, although shoaling over shallow ridges on the western and northern sides of the island produces high-frequency nonlinear wave energy that radiates away. High-frequency radiating energy is also generated due to lee-wave generation by strong barotropic tides in these regions, although it is difficult to distinguish between lee-wave generation and resonance and shoaling.

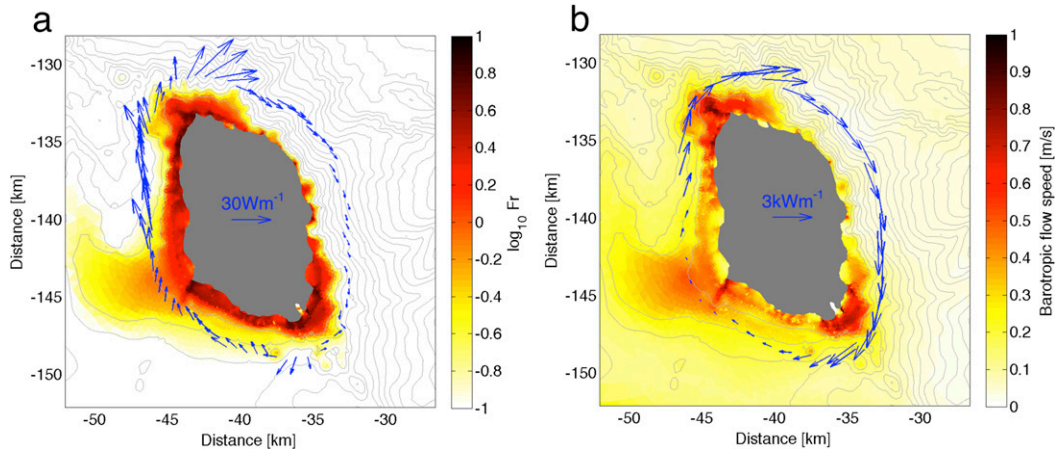Most studies on internal tides focus on the semidiurnal band because semidiurnal tides dominate in most of the

FIG. 16. (a) High-pass and (b) low-pass filtered baroclinic internal wave energy flux vectors around Izu-Oshima Island for the K_1 forcing case plotted over (a) the maximum Froude number on a $\log_{10}$ scale and (b) the maximum barotropic flow speed. The cutoff filter frequency is $3\omega_{K1}$. Bathymetry contours are spaced at 100-m intervals.

world's oceans (e.g., Wunsch 1975; Morozov 1995; Cacchione et al. 2002). However, the results in this paper point to the importance of trapped diurnal internal tides, which can resonate around midlatitude islands and produce more energy flux than the semidiurnal internal tides. The trapped internal tides can have a significant impact on local turbulence and mixing processes, while nonlinear effects can lead to the generation of higher-frequency waves that radiate from the islands. These can act as a potential source for remote turbulence and mixing and enhance transport of sediments, nitrates, and organic material from the coastal ocean into the ocean interior (e.g., McPhee-Shaw 2006, Masunaga et al. 2017). Given the ubiquity of small islands and complex topography at midlatitudes, trapped diurnal internal waves could be an important contributor to coastal ocean transport and mixing through much of the world's oceans.

APPENDIX

Model Validation: Computational Details

a. Adjusting boundary forcing

To model the observed tidal elevations, the amplitude of the barotropic tidal forcing at the boundary A [in (9)] was adjusted with a Newton method to minimize the error between the observed and modeled tidal amplitudes. The error in the tidal amplitude in the model is represented as

$$e(A^j) = a^j_{\text{model}} - a^j_{\text{obs}}, \qquad (A1)$$

where A is the forcing component, j is the tidal constituent (S_2, M_2, K_1, and O_1), and model and obs denote modeled and observed quantities, respectively. In the Newton method, a new guess for the boundary forcing at iteration $k + 1$ based on old values k is given by

$$A^j_{k+1} = A^j_k - \frac{e\left(A^j_k\right)}{e'\left(A^j_k\right)}, \qquad (A2)$$

where the derivative of the error is computed from two previous model guesses with

$$e'(A^j_k) = \frac{\Delta e^j_k}{\Delta A^j_k} = \frac{e^j_k - e^j_{k-1}}{A^j_k - A^j_{k-1}} = \frac{a^j_k - a^j_{k-1}}{A^j_k - A^j_{k-1}}. \qquad (A3)$$

The method begins with an initial estimate A_1 from (5) and the iteration proceeds until the absolute value of the error [(A2)] satisfies $|e(A)| < 10^{-3}$ m.

b. Additional tidal validation for phase

To validate the propagation of surface tidal waves, we compared the tidal phase of K_1 and M_2 reproduced in the model (runs 2 and 3) with the TPXO8 tidal model (Egbert and Erofeeva 2002). Results from both SUNTANS and TPXO8 (Fig. A1) show that surface tidal waves propagate toward the east around Izu-Oshima Island and over Izu–Ogasawara Ridge for both
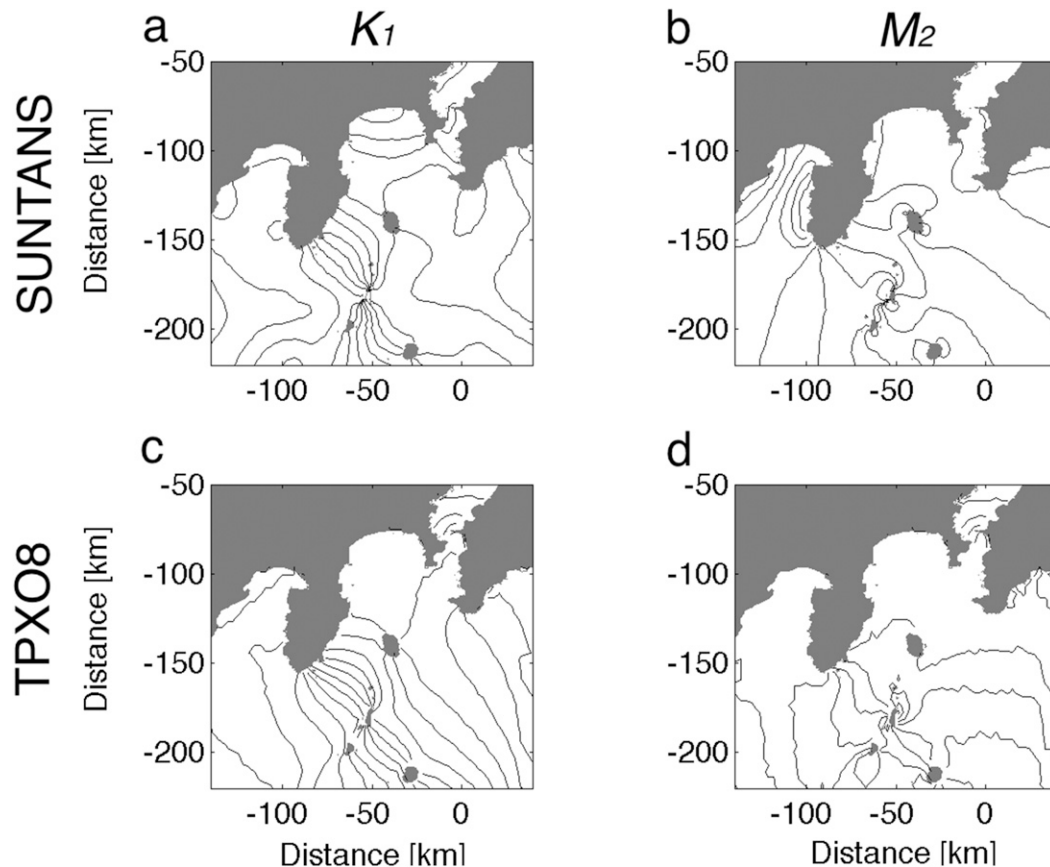
FIG. A1. Tidal phase from (a),(b) SUNTANS and (c),(d) the TPXO tidal model for the (left) M_2 and (right) K_1 tidal constituents at intervals of 1° for M_2 and 2° for K_1.

semidiurnal and diurnal tidal constituents, which is consistent with tidal phases shown by Ohwaki et al. (1991). In addition, the phase speed (interval of phase contour lines) is similar for SUNTANS and TPXO8. However, inconsistencies appear in Sagami Bay for the semidiurnal case and Suruga Bay for the diurnal case. Such inconsistencies may be due to simplified bathymetry and tidal forcing. These effects may not strongly influence internal waves near the island and would likely not change the findings related to the internal wave dynamics and energetics presented in this paper.

REFERENCES

Allen, J., P. Somerfield, and F. Gilbert, 2007: Quantifying uncertainty in high-resolution coupled hydrodynamic-ecosystem models. *J. Mar. Syst.*, **64**, 3–14, doi:10.1016/j.jmarsys.2006.02.010.

Auger, G., H. Yamazaki, T. Nagai, C. Jiao, and M. Kumagai, 2013: Hypolimnetic turbulence generation associated with super-position of large-scale internal waves in a strongly stratified lake: Lake Biwa, Japan. *Limnology*, **14**, 229–238, doi:10.1007/s10201-013-0401-4.

Bell, T. H., 1975: Lee waves in stratified flows with simple harmonic time dependence. *J. Fluid Mech.*, **67**, 705–722, doi:10.1017/S0022112075000560.

Brink, K. H., 1999: Island-trapped waves, with application to observations off Bermuda. *Dyn. Atmos. Oceans*, **29**, 93–118, doi:10.1016/S0377-0265(99)00003-2.

Buijsman, M. C., and Coauthors, 2016: Impact of parameterized internal wave drag on the semidiurnal energy balance in a global ocean circulation model. *J. Phys. Oceanogr.*, **46**, 1399–1419, doi:10.1175/JPO-D-15-0074.1.

Cacchione, D. A., L. F. Pratson, and A. S. Ogston, 2002: The shaping of continental slopes by internal tides. *Science*, **296**, 724–727, doi:10.1126/science.1069803.

Caldwell, D. R., and S. A. Eide, 1976: Experiments on the resonance of long-period waves near islands. *Proc. Roy. Soc. London*, **A348**, 359–378, doi:10.1098/rspa.1976.0043.

Carter, G. S., 2010: Barotropic and baroclinic M_2 tides in the Monterey Bay region. *J. Phys. Oceanogr.*, **40**, 1766–1783, doi:10.1175/2010JPO4274.1.

——, and M. C. Gregg, 2002: Intense, variable mixing near the head of Monterey Submarine Canyon. *J. Phys. Oceanogr.*, **32**, 3145–3165, doi:10.1175/1520-0485(2002)032<3145:IVMNTH>2.0.CO;2.

Dauxois, T., and W. R. Young, 1999: Near-critical reflection of internal waves. *J. Fluid Mech.*, **390**, 271–295, doi:10.1017/S0022112099005108.

Egbert, G. D., and S. Y. Erofeeva, 2002: Efficient inverse modeling of barotropic ocean tides. *J. Atmos. Oceanic Technol.*, **19**, 183–204, doi:10.1175/1520-0426(2002)019<0183:EIMOBO>2.0.CO;2.

Farmer, D., and L. Armi, 1999: Stratified flow over topography: The role of small-scale entrainment and mixing in flow establishment. *Proc. Roy. Soc. London*, **A455**, 3221–3258, doi:10.1098/rspa.1999.0448.

Fringer, O. B., M. Gerritsen, and R. L. Street, 2006: An unstructured-grid, finite-volume, nonhydrostatic, parallel coastal ocean simulator. *Ocean Modell.*, **14**, 139–173, doi:10.1016/j.ocemod.2006.03.006.

Garrett, C., and E. Kunze, 2007: Internal tide generation in the deep ocean. *Annu. Rev. Fluid Mech.*, **39**, 57–87, doi:10.1146/annurev.fluid.39.050905.110227.

Gill, A. E., and A. J. Clarke, 1974: Wind-induced upwelling, coastal currents and sea-level changes. *Deep-Sea Res. Oceanogr. Abstr.*, **21**, 325–345, doi:10.1016/0011-7471(74)90038-2.

Gille, S. T., S. G. Llewellyn Smith, and S. M. Lee, 2003: Measuring the sea breeze from QuikSCAT scatterometry. *Geophys. Res. Lett.*, **30**, 1114, doi:10.1029/2002GL016230.

Halpern, D., 1971: Observations on short period internal waves in Massachusetts Bay. *J. Mar. Res.*, **29**, 116–132.

Hibiya, T., 1986: Generation mechanism of internal waves by tidal flow over a sill. *J. Geophys. Res.*, **91**, 7697–7708, doi:10.1029/JC091iC06p07697.

Hogg, N. G., 1980: Observations of internal Kelvin waves trapped round Bermuda. *J. Phys. Oceanogr.*, **10**, 1353–1376, doi:10.1175/1520-0485(1980)010<1353:OOIKWT>2.0.CO;2.

Igeta, Y., K. Yamazaki, and T. Watanabe, 2015: Amplification of coastal-trapped waves resonantly generated by wind around Sado Island, Japan. *J. Oceanogr.*, **71**, 41–51, doi:10.1007/s10872-014-0259-z.

Jordi, A., G. Basterretxea, and D.-P. Wang, 2009: Evidence of sediment resuspension by island trapped waves. *Geophys. Res. Lett.*, **36**, L18610, doi:10.1029/2009GL040055.

Kang, D., and O. Fringer, 2012: Energetics of barotropic and baroclinic tides in the Monterey Bay area. *J. Phys. Oceanogr.*, **42**, 272–290, doi:10.1175/JPO-D-11-039.1.

Kitade, Y., and M. Matsuyama, 1997: Characteristics of internal tides in the upper layer of Sagami Bay. *J. Oceanogr.*, **53**, 143–159.

——, and ——, 2000: Coastal-trapped waves with several-day period caused by wind along the southeast coast of Honshu, Japan. *J. Oceanogr.*, **56**, 727–744, doi:10.1023/A:1011186018956.

Kozlov, I., D. Romanenkov, A. Zimin, and B. Chapron, 2014: SAR observing large-scale nonlinear internal waves in the White Sea. *Remote Sens. Environ.*, **147**, 99–107, doi:10.1016/j.rse.2014.02.017.

Kundu, P. K., 1990: *Fluid Mechanics*. Academic Press, 638 pp.

Le Provost, C., M. L. Genco, F. Lyard, P. Vincent, and P. Canceil, 1994: Spectroscopy of the world ocean tides from a finite element hydrodynamic model. *J. Geophys. Res.*, **99**, 24 777–24 797, doi:10.1029/94JC01381.

Longuet-Higgins, M. S., 1969: On the trapping of long-period waves round islands. *J. Fluid Mech.*, **37**, 773–784, doi:10.1017/S0022112069000875.

——, 1970: Steady currents induced by oscillations round islands. *J. Fluid Mech.*, **42**, 701–720, doi:10.1017/S0022112070001568.

Masunaga, E., H. Homma, H. Yamazaki, O. B. Fringer, T. Nagai, Y. Kitade, and A. Okayasu, 2015: Mixing and sediment resuspension associated with internal bores in a shallow bay. *Cont. Shelf Res.*, **110**, 85–99, doi:10.1016/j.csr.2015.09.022.

——, R. S. Arthur, O. B. Fringer, and H. Yamazaki, 2017: Sediment resuspension and generation of intermediate nephew layers by shoaling internal bores. *J. Mar. Syst.*, **170**, 31–41, doi:10.1016/j.jmarsys.2017.01.017.

McPhee-Shaw, E., 2006: Boundary–interior exchange: Reviewing the idea that internal-wave mixing enhances lateral dispersal near continental margins. *Deep-Sea Res. II*, **53**, 42–59, doi:10.1016/j.dsr2.2005.10.018.

Mihanović, H., G. B. Paklar, and M. Orlić, 2014: Resonant excitation of island-trapped waves in a shallow, seasonally stratified sea. *Cont. Shelf Res.*, **77**, 24–37, doi:10.1016/j.csr.2014.01.014.

Millero, F. J., and A. Poisson, 1981: International one-atmosphere equation of state of seawater. *Deep-Sea Res.*, **28A**, 625–629, doi:10.1016/0198-0149(81)90122-9.

Morozov, E. G., 1995: Semidiurnal internal wave global field. *Deep-Sea Res. I*, **42**, 135–148, doi:10.1016/0967-0637(95)92886-C.

Moum, J. N., D. M. Farmer, W. D. Smyth, L. Armi, and S. Vagle, 2003: Structure and generation of turbulence at interfaces strained by internal solitary waves propagating shoreward over the continental shelf. *J. Phys. Oceanogr.*, **33**, 2093–2112, doi:10.1175/1520-0485(2003)033<2093:SAGOTA>2.0.CO;2.

Munk, W., and C. Wunsch, 1998: Abyssal recipes II: Energetics of tidal and wind mixing. *Deep-Sea Res.*, **45**, 1977–2010, doi:10.1016/S0967-0637(98)00070-3.

Murphy, A. H., 1988: Skill scores based on the mean square error and their relationships to the correlation coefficient. *Mon. Wea. Rev.*, **116**, 2417–2424, doi:10.1175/1520-0493(1988)116<2417:SSBOTM>2.0.CO;2.

Nakatsuka, T., M. Toda, K. Kawamura, and M. Wakatsuchi, 2004: Dissolved and particulate organic carbon in the Sea of Okhotsk: Transport from continental shelf to ocean interior. *J. Geophys. Res.*, **109**, C09S14, doi:10.1029/2003JC001909.

Niwa, Y., and T. Hibiya, 2004: Three-dimensional numerical simulation of M_2 internal tides in the East China Sea. *J. Geophys. Res.*, **109**, C04027, doi:10.1029/2003JC001923.

Ohwaki, A., M. Matsuyama, and S. Iwata, 1991: Evidence for predominance of internal tidal currents in Sagami and Suruga Bays. *J. Oceanogr. Soc. Japan*, **47**, 194–206, doi:10.1007/BF02310035.

Pawlowicz, R., B. Beardsley, and S. Lentz, 2002: Classical tidal harmonic analysis with errors in MATLAB using T-TIDE. *Comput. Geosci.*, **28**, 929–937, doi:10.1016/S0098-3004(02)00013-4.

Pond, S., and G. L. Pickard, 1983: *Introductory Dynamical Oceanography*. 2nd ed. Pergamon Press, 329 pp.

Rainville, L., and R. Pinkel, 2006: Baroclinic energy flux at the Hawaiian Ridge: Observations from the R/P *FLIP*. *J. Phys. Oceanogr.*, **36**, 1104–1122, doi:10.1175/JPO2882.1.

Richards, C., D. Bourgault, P. S. Galbraith, A. Hay, and D. E. Kelley, 2013: Measurements of shoaling internal waves and turbulence in an estuary. *J. Geophys. Res. Oceans*, **118**, 273–286, doi:10.1029/2012JC008154.

Saggio, A., and J. Imberger, 1998: Internal wave weather in a stratified lake. *Limnol. Oceanogr.*, **43**, 1780–1795, doi:10.4319/lo.1998.43.8.1780.

Sharples, J., C. M. Moore, A. E. Hickman, P. M. Holligan, J. F. Tweddle, M. R. Palmer, and J. H. Simpson, 2009: Internal tidal mixing as a control on continental margin ecosystems. *Geophys. Res. Lett.*, **36**, L23603, doi:10.1029/2009GL040683.

Tanaka, Y., T. Hibiya, Y. Niwa, and N. Iwamae, 2010: Numerical study of K_1 internal tides in the Kuril straits. *J. Geophys. Res.*, **115**, C09016, doi:10.1029/2009JC005903.

Thorpe, S. A., 1987: Transitional phenomena and the development of turbulence in stratified fluids: A review. *J. Geophys. Res.*, **92**, 5231–5248, doi:10.1029/JC092iC05p05231.

——, 1998: Some dynamical effects of internal waves and the sloping sides of lakes. *Physical Processes in Lakes and Oceans*, Coastal and Estuarine Studies, Vol. 54, Amer. Geophys. Union, 441–460, doi:10.1029/CE054p0441.

Vitousek, S., and O. B. Fringer, 2011: Physical vs. numerical dispersion in nonhydrostatic ocean modeling. *Ocean Modell.*, **40**, 72–86, doi:10.1016/j.ocemod.2011.07.002.

Walsh, J. J., 1991: Importance of continental margins in the marine biogeochemical cycling of carbon and nitrogen. *Nature*, **350**, 53–55, doi:10.1038/350053a0.

Wunsch, C., 1975: Internal tides in the ocean. *Rev. Geophys.*, **13**, 167–182, doi:10.1029/RG013i001p00167.

Zhang, Z., O. B. Fringer, and S. R. Ramp, 2011: Three-dimensional, nonhydrostatic numerical simulation of nonlinear internal wave generation and propagation in the South China Sea. *J. Geophys. Res.*, **116**, C05022, doi:10.1029/2010JA016287.

Zilberman, N. V., J. M. Becker, M. A. Merrifield, and G. S. Carter, 2009: Model estimates of M_2 internal tide generation over mid-Atlantic Ridge topography. *J. Phys. Oceanogr.*, **39**, 2635–2651, doi:10.1175/2008JPO4136.1.